

The unexpected radiative impact of the Hunga Tonga eruption of January 15th, 2022

Pasquale Sellitto (✉ pasquale.sellitto@lisa.ipsl.fr)

Univ. Paris Est Créteil and Université de Paris-Cité, CNRS, Laboratoire Interuniversitaire des Systèmes Atmosphériques (LISA-IPSL), Institut Pierre Simon Laplace <https://orcid.org/0000-0001-7440-2350>

Aurelien Podglajen

Laboratoire de Météorologie Dynamique

Redha Belhadji

Univ. Paris Est Créteil and Université de Paris-Cité, CNRS, Laboratoire Interuniversitaire des Systèmes Atmosphériques (LISA-IPSL), Institut Pierre Simon Laplace

Marie Boichu

Elisa Carboni

UK Research and Innovation, Science and Technology Facilities Council, Rutherford Appleton Laboratory

Juan Cuesta

Univ. Paris Est Créteil and Université de Paris-Cité, CNRS, Laboratoire Interuniversitaire des Systèmes Atmosphériques (LISA-IPSL), Institut Pierre Simon Laplace

Clair Duchamp

Laboratoire de Météorologie Dynamique (LMD-IPSL), UMR CNRS 8539, ENS-PSL, École Polytechnique, Sorbonne Université, Institut Pierre Simon Laplace

Corinna Kloss

Laboratoire de Physique de l'Environnement et de l'Espace, CNRS UMR 7328, Université d'Orléans

Richard Siddans

UK Research and Innovation, Science and Technology Facilities Council, Rutherford Appleton Laboratory

Nelson Begue

Luc Blarel

Univ. Lille, CNRS, UMR 8518 – LOA – Laboratoire d'Optique Atmosphérique

Fabrice Jegou

Laboratoire de Physique et Chimie de l'Environnement et de l'Espace (LPC2E), UMR 7328 CNRS-Université d'Orléans

Sergey Khaykin

Laboratoire Atmospheres, Observations Spatiales (LATMOS)

Jean-Baptiste Renard

Laboratoire de Physique de l'Environnement et de l'Espace, CNRS UMR 7328, Université d'Orléans

Bernard Legras

CNRS / PSL-ENS, Sorbonne Université, Ecole Polytechnique <https://orcid.org/0000-0002-3756-7794>

Article

Keywords:

Posted Date: April 18th, 2022

DOI: <https://doi.org/10.21203/rs.3.rs-1562573/v1>

License:   This work is licensed under a Creative Commons Attribution 4.0 International License.

[Read Full License](#)

Additional Declarations: There is **NO** Competing Interest.

Version of Record: A version of this preprint was published at Communications Earth & Environment on November 19th, 2022. See the published version at <https://doi.org/10.1038/s43247-022-00618-z>.

23 **Abstract**

24 The underwater Hunga Tonga-Hunga Ha-apai (HT) volcano violently erupted on January 15th,
25 2022, injecting volcanic gases and aerosols at over 50 km altitude. Here we show the
26 stratospheric aerosol and water vapour perturbations due to the HT eruption, the plume evolution
27 during the first month dispersion and we estimate its short-term radiative impact. The HT
28 eruption produced the largest perturbation of stratospheric aerosols and water vapour since the
29 eruption of Pinatubo volcano in 1991. During the first three weeks following the eruption, water
30 vapour radiative cooling dominates the plume's heating/cooling rates, reaching values as large as
31 -10 K/d and produces a fast plume descent of several km. At the top-of-the-atmosphere (TOA)
32 and surface, volcanic aerosol cooling dominates the radiative forcing (RF) for the fresh plume.
33 After two weeks, due to dispersion/dilution, water vapour heating starts to dominate the TOA
34 RF, leading to a net warming of the climate system, which was never reported before for a
35 volcanic plume. The surface RF, on the contrary, is dominated by the aerosol effect and reaches
36 values of near -2 Wm^{-2} , exceeding the hemispheric-averaged surface impact of stratospheric
37 events of the last 30 years.

38 **Main**

39 Major volcanic eruptions emit gas and aerosol pollutants into the stratosphere, that can impact on
40 the atmospheric radiative balance and the climate system^{1,2,3}. After a phase of volcanic unrest
41 starting from end December 2021, and strong explosions on January 14th, 2022 removing the
42 aerial part of the volcano, the submarine Hunga Tonga–Hunga Ha'apai (HT) volcano (20.57°S,
43 175.38°W) violently erupted on January 15th, 2022, at approximately 04:15 UTC. The eruption
44 produced tsunamis over a large area of the Pacific Ocean, as far as Peru
45 (<https://www.bbc.com/news/av/world-asia-60018707>), and atmospheric shockwaves that
46 propagated around the globe^{4,5}. Based on stereoscopic geostationary satellite observations, the
47 volcanic plume summit was observed at altitudes over 50 km, a record since the Pinatubo
48 (Philippines) eruption in 1991⁶. Volcanic ash, gas and water vapour were injected at these
49 unprecedented altitudes, well into the stratosphere and up to the lower mesosphere. Nevertheless,
50 first estimations indicated a total burden of the injected sulphur dioxide (SO₂) of about 0.4 Tg⁷.
51 This is far less than the injected mass for the climate-significant Pinatubo eruption (Philippines,
52 1991), estimated at values as large as $19 \pm 4 \text{ Tg}^8$, or even the more recent moderate stratospheric

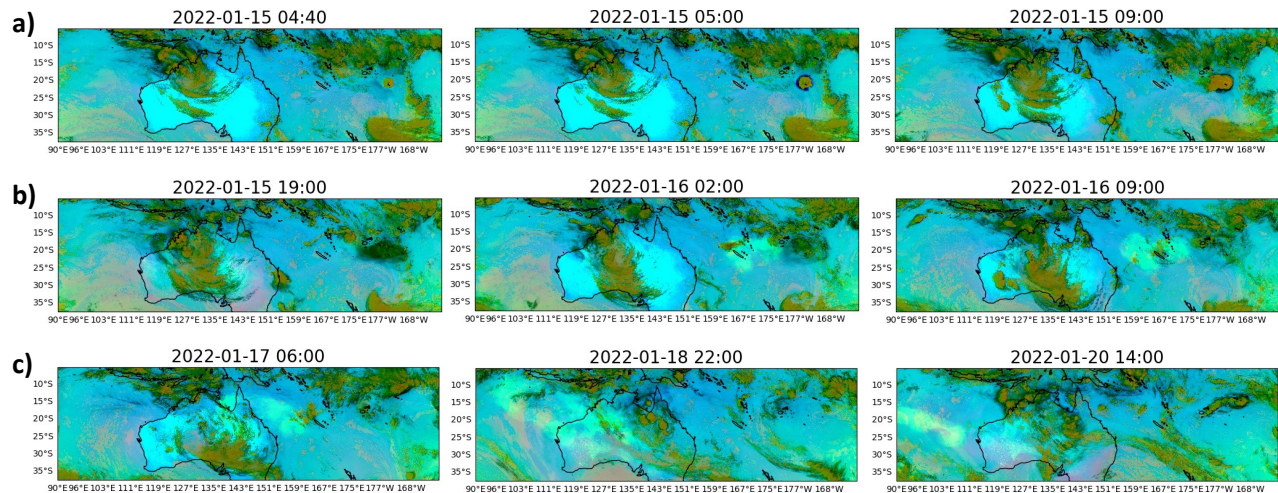
53 Raikoke 2019 ($1.5 \pm 0.2 \text{ Tg}^9$) or Nabro 2011 eruptions (1.6 Tg^{10}). Based on this evidence, it was
54 initially suggested that the impact of HT on the stratospheric aerosol layer and climate is
55 negligible⁷.

56 In contrast with these initial conclusions, here we show that the HT eruption of January 15th,
57 2022 produced an exceptionally large stratospheric aerosol and water vapour perturbations, that
58 in turns have produced large perturbations on the atmospheric radiation budget, with significant
59 impacts on the plume dynamics and the climate system.

60 **Injection, initial dispersion, atmospheric evolution and optical properties of the HT aerosol** 61 **plume**

62 Using the high spatial and temporal resolution of geostationary satellite instruments (Himawari
63 Ash RGB product, see Methods), the first phases of the HT eruption can be followed (Fig. 1).
64 The HT volcano violently erupted on January 15th, at 04:15. A volcanic umbrella forms during
65 the first hours after the eruption. At this stage, the localized plume is dominated by ash and water
66 condensates (liquid water and ice crystals), as visible in black/brownish, in Fig. 1, row (a). A
67 sulphur-rich plume gradually separates on the western side starting from January 15th, at 19:00.
68 While the ash/ice component stays local and gradually dissipates due to sedimentation
69 (brownish/black plume in Fig. 1, row (b)), the sulphur-rich plume's component is advected
70 towards the west (greenish plume in Fig. 1, row (b)). Notice the absence of red, reddish or
71 yellow colours that would indicate a thin ash plume or a mixture of ash and sulphur compounds.
72 Over January 16th-18th, the sulphur-dominated plume moves across Australia and then towards
73 the southern Indian Ocean afterwards (Fig. 1, row (c)). We stress that this satellite product
74 cannot distinguish between SO₂ and sulphate aerosols, which have overlapping spectral
75 signatures in this spectral range and both appear as green¹¹. A comparison of Ash RGB
76 Himawari images and SO₂ and sulphate-specific aerosol optical depth (AOD) from IMS/IASI
77 satellite observations (see Methods) shows that most of the greenish plume observed in Fig. 1 is
78 composed of secondary sulphate aerosols rather than SO₂. This hints at an exceptionally rapid
79 conversion of volcanic SO₂ primary emissions to secondary sulphate aerosols and may explain
80 why the retrieved total SO₂ emitted mass is relatively small while the stratospheric aerosol
81 perturbation is large. One reason for the rapid conversion of SO₂ to secondary sulphate aerosols
82 may be the extremely large availability of water vapour (see Section "The water vapour plume")

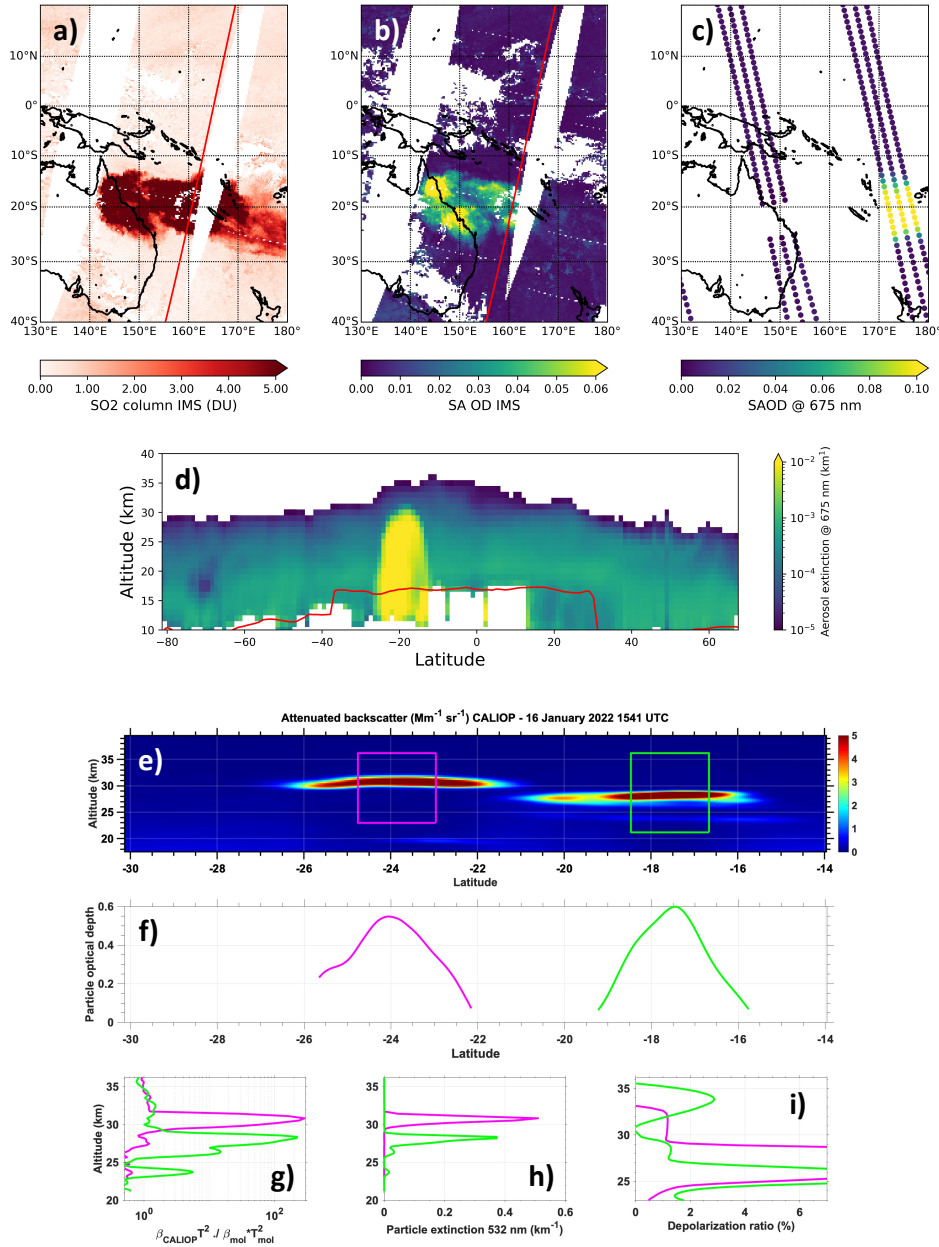
83 and ref. 12). The rate of SO₂-to-aerosol formation, at stratospheric temperature conditions,
84 depends strongly on the relative humidity, larger humidity linked to quicker secondary sulphate
85 aerosols formation¹³.



86 **Figure 1: Volcanic injection and initial HT plume evolution.** *Selected Ash RGB Himawari*
87 *images for three sequences of the initial dispersion of the HT volcanic plume (January 15th at*
88 *4:40 to January 20th at 14:00). Row (a): HT explosion and plume rise; row (b): quick ash*
89 *sedimentation; row (c) sulphur-rich plume dispersion across Australia. All times are UTC. By a*
90 *RGB band combination, this product allows to qualitatively distinguish thick ash plumes or ice*
91 *clouds (brown), thin ice clouds (dark blue) and sulphur-containing plumes (green). Mixed*
92 *ash/sulphur-containing volcanic species would appear in reddish and yellow shades.*

93 Observations with high vertical resolution space LiDAR CALIOP (see Methods) confirm this
94 initial evolution of the HT aerosol plume. A first overpass on January 15th reveals the presence
95 of aspherical particles within the plume (Fig. S1), i.e. ash and/or ice crystals, at altitudes between
96 34 km and the maximum range of CALIOP observations at 40 km. At this stage, large SO₂
97 content (>5 Dobson Units) is observed by IMS/IASI, with simultaneous small sulphate-specific
98 AOD (<0.04). A relatively large total AOD is observed by the localized in-plume CALIOP
99 observations (0.26) and by the stratospheric-integrated OMPS-LP AOD (SAOD, see Methods)
100 satellite observations (~0.2), thus indicating the presence of non-sulphate aerosols. The situation
101 is very different for the CALIOP overpass of the following day, January 16th (Fig. 2). By then,
102 the depolarization is already as low as 2% (with larger values only at the bottom of the plume),
103 pointing at the increasing presence of spherical particles. These evidences can be linked to the

104 rapid ash rapid deposition and formation of secondary sulphate aerosols. This is confirmed by an
105 increase in IMS/IASI sulphate-specific AOD (~ 0.1 in frontal sections of the plume, see Fig. 2b).
106 Exceptionally large in-plume AOD values of almost 0.5 in the visible spectral range are observed
107 by CALIOP. This can almost entirely be attributed to sulphate aerosols.
108 Ground-based aerosol sun-photometric observations from the AERONET network (see Methods)
109 confirm the overpass of the plume in Australia and beyond, and an evolution towards small and
110 reflective (single scattering albedo ~ 0.98 at 440 nm) sulphate aerosols, during this initial
111 dispersion phase (Fig. S2). The overpass of a plume dominated by fine aerosols is observed over
112 eastern Australia (Lucinda AERONET station) starting on January 16th and then, two days later,
113 over western Australia (Learmonth AERONET station), with fine-mode-specific AOD > 0.5 at
114 ~ 500 nm. The evolution observed from the ground is consistent with satellite observations, i.e.
115 Himawari timing and CALIOP aerosol burden. Observations from IMS/IASI show that the
116 plume is quickly transported westward over the Indian Ocean and a corresponding increase in
117 fine mode AOD is observed from the ground at La Réunion island (Réunion Saint Denis and
118 Maïdo OPAR AERONET stations) starting from January 22nd, with slightly reduced AODs
119 (peak value ~ 0.6) due to plume dilution. A rapid-response balloon campaign was carried out at
120 La Réunion to observe the young dispersed HT plume. In situ LOAC aerosol optical
121 observations (see Methods) show enhanced aerosol extinction values at around 22 and 25 km
122 altitude, composed of submicron, mainly semi-transparent (liquid) aerosol particles (Fig. S3).



123

124 **Figure 2: The physicochemical properties of the early HT plume .** *IMS/IASI SO2 (panel a)*
 125 *and sulphate-specific AOD (panel b) observations for January 16th at 23:07 UTC. In panel a*
 126 *and b, the red line is CALIOP track for the same day at 15:41 UTC. OMPS-LP integrated SAOD*
 127 *(panel c) and vertical aerosol extinction profile (central detector, panel d) for January 16th at*
 128 *2:03 and 3:27 UTC. In panel d, the red line is tropopause height. Attenuated CALIOP*
 129 *backscatter at 532 nm (panel e), and integrated in-plume AOD (panel f), corrected transmission*
 130 *(panel g), extinction (panel h) and depolarization (panel i) in the two identified plumes sections*

131 *(pink and green squares). The CALIOP track of panels e-i is the one identified in panels a and b.*
132 *Due to the time mismatch between CALIOP and IASI orbits, the CALIOP trace actually crossed*
133 *both the eastern part of the aerosol plume in panels a-b (lower plume at 27 km) and the western*
134 *part (upper plume at 30 km) which has already reached Australia in the display.*

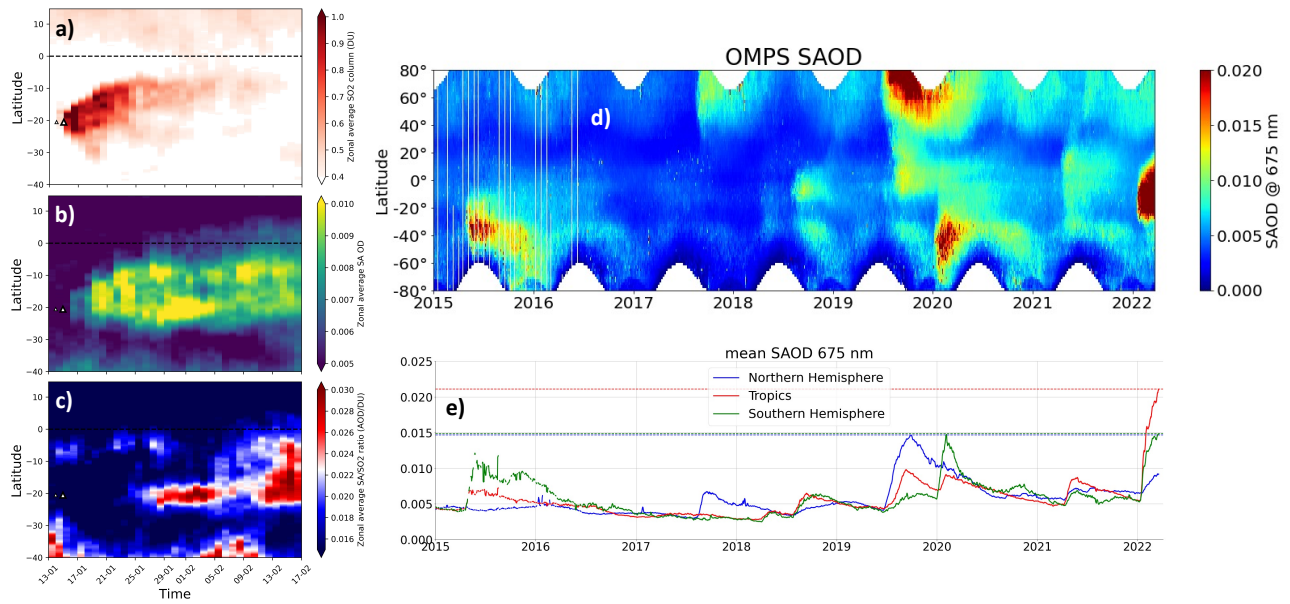
135 Over the following weeks, the HT plume is quickly advected zonally across the globe,
136 circumnavigated the Earth and is observed again in Australia at the end of January 2022. Peak
137 optical depths of ~ 0.2 are repetitively observed by CALIOP, e.g. on February 8th (Fig. S4), with
138 very small depolarization ratio ($< 2\%$), confirming that the dispersed plume is largely dominated
139 by spherical sulphate aerosols. Relatively large colour ratio might indicate an increase in aerosol
140 size due to sulphate aerosols water uptake/coagulation processes.

141 **Impact on the global stratospheric aerosol layer**

142 Using time series of satellite observations, insights into the HT plume longer-term evolution and
143 the comparison of its impact with recent stratospheric eruptions can be obtained. A clear but
144 limited enhancement of SO₂, with respect to background SO₂ levels, is visible from zonal
145 average IMS/IASI SO₂ observations (Fig. 3a). The sulphate aerosol plume starts to form very
146 quickly, with an enhancement already visible on January 16th (zonal average sulphate-specific
147 AOD in Fig. 3b). The sulphate aerosol formation is very sustained and the sulphate-specific
148 AOD zonal averages quickly reach values as large as 0.01. This is a large value because: 1) it is
149 zonally averaged over the whole globe and 2) IMS/IASI sulphate-specific AOD retrievals are in
150 the mid-infrared, which translates into much larger sulphate-specific AOD values in the visible
151 spectral range. Two different plume branches can be observed (Fig. 3a-c): a northern branch,
152 with slower sulphate aerosol formation and a southern branch, with quicker sulphate aerosol
153 formation and a rapid consumption of SO₂. Overall, the HT plume dispersed quickly over the
154 global southern hemispheric tropics and limited parts of the plume crossed the equator,
155 enhancing the stratospheric aerosol layer also in the Northern Hemisphere. This is a quite
156 singular dispersion dynamics compared to recent stratospheric events, whose dispersion was
157 largely poleward^{14,15}. The relatively fast HT plume cross-equatorial dispersion might be due to
158 the particularly high altitude of the injection for this eruption.

159 Time series of OMPS-LP SAOD show that the HT eruption has produced the largest peak SAOD
160 perturbation during its OMPS mission (Fig. 3d), larger than, e.g., the Raikoke eruption 2019¹⁵

161 and the Australian fires 2019-2020¹⁴. The mean impact on the tropical and Southern Hemispheric
 162 stratosphere is the largest observed by OMPS-LP (tropical average: ~ 0.22 , Southern
 163 Hemispheric average: ~ 0.15 , on par with the Australian fires 2019-2020) (Fig. 3b). The
 164 Australian fires 2019-2020 was previously considered the largest SAOD perturbation since
 165 Pinatubo eruption in 1991¹⁴ so our result on HT can be extended backwards: the impact of the
 166 HT eruption on the stratospheric aerosol layer is the strongest since Pinatubo 1991.



167

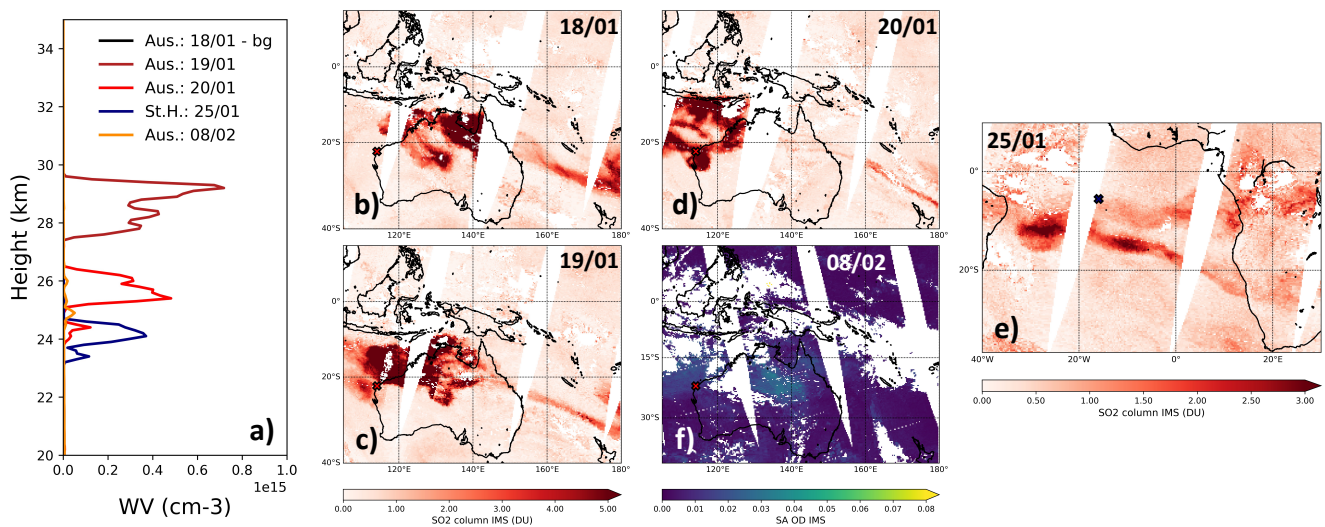
168 **Figure 3: Longer-term HT plume evolution and its comparison with recent past events.**

169 *Zonal average IMS/IASI SO₂ observations (panel a), sulphate-specific AOD (panel b) and their*
 170 *ratio (panel c). Black triangles in panels a-c indicate the main HT eruption of January 15th*
 171 *(large triangle) and the previous smaller event of January 14th (that had a small but visible*
 172 *impact on the SO₂ distributions). Time series of the OMPS-LP zonal average SAOD (panel d)*
 173 *and tropical (30°N-30°S, red line), Northern Hemisphere (0-80°N, blue line) and Southern*

174 Hemisphere (0-80°S green line) SAOD (panel e). Red, blue and green dotted horizontal lines, in
175 panel e, are the absolute maxima in the time series, in the three latitude bands.

176 The water vapour plume

177 The underwater HT eruption injected a huge amount of water vapour into the stratosphere. This
178 is due to both volcanic caldera intrusion of seawater (G. Carazzo, personal communication) and
179 mechanical interaction with seawater, over the underwater eruptive crater, during the eruption.
180 As a result, record-breaking water vapour content is found in the stratosphere, within the plume,
181 with radio-soundings (see Methods). Water vapour concentrations exceed 0.5-0.8 molecules cm^{-3}
182 (up to over 1500 ppmv) for the fresh plume over Australia on January 19th-20th, 0.4 molecules
183 cm^{-3} (~500 ppmv) for the dispersed plume at Saint Helena Island on January 25th, and 0.1
184 molecules cm^{-3} (~100 ppmv) after a full circumnavigation of the Earth, back over Australia on
185 February 8th (Fig. 4a).



186 **Figure 4: Water vapour in the HT plume.** Water vapour radio-sounding observations over
187 western Australia on January 18th (unperturbed background in RF estimations, black line), 19th
188 (dark red line), 20th (red line), and February 8th (yellow line), and over Saint Helena island
189 (blue line) (panel a). Plume and sounding positions (red crosses) are shown in panels b-e, using
190 IMS/IASI SO₂ and sulphate-specific AOD observations.

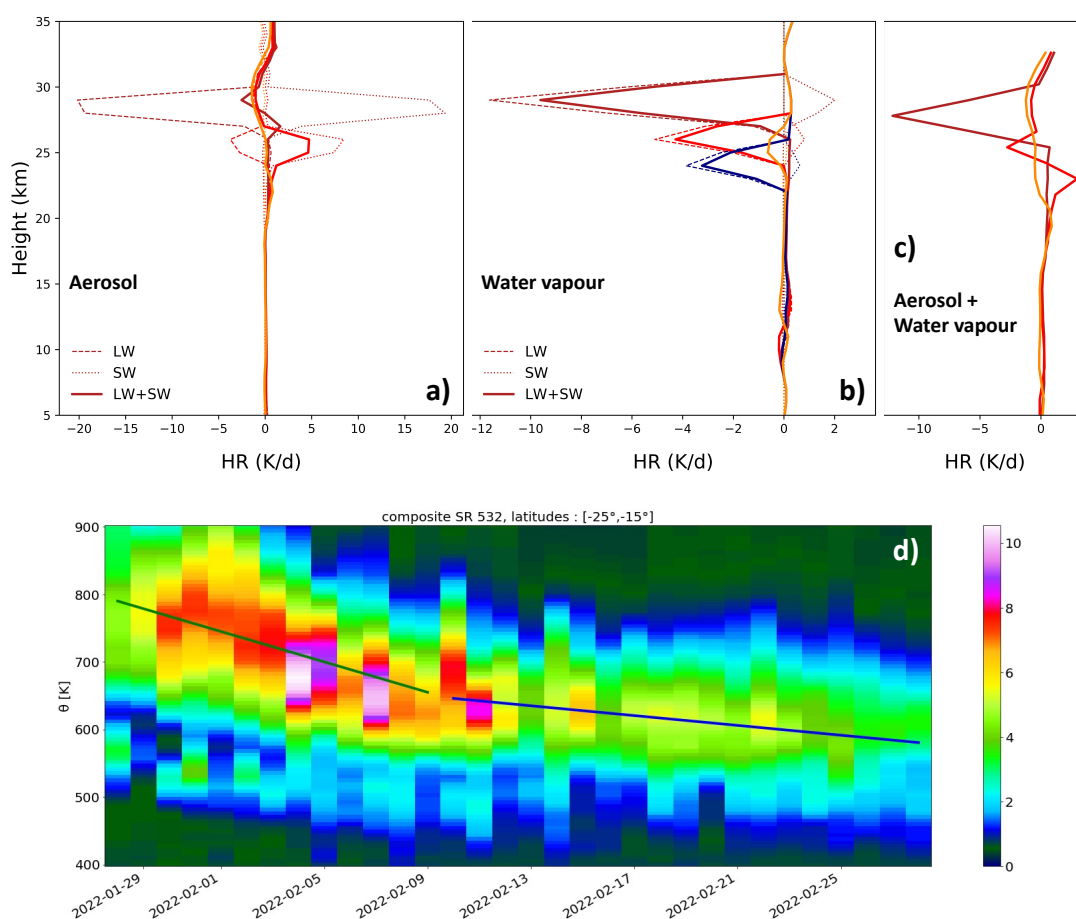
191 Radiative impacts of the aerosol and water vapour plume

192 Localised stratospheric radiative heating/cooling due to aerosol and water vapour perturbation
193 from the HT plume are calculated with offline radiative transfer (RT) modelling (see Methods).

194 Three plume-perturbed cases are considered, using CALIOP in-plume extinction observations: 1)
195 fresh plume, higher section (average aerosol extinction in the pink box of Fig. 2, January 16th
196 overpass); 2) fresh plume, lower section (average aerosol extinction in the green box of Fig. 2,
197 January 16th overpass); 3) aged plume, after a full global zonal circumnavigation (average
198 aerosol extinction in the green box of Fig. S4, February 8th overpass). Based on the plume
199 evolution discussed above, aerosol layers are simulated as small and very-weakly-absorbing (to
200 account for a possible very small residual ash fraction) sulphate particles, for the fresh plume,
201 with a small increase in size due to condensation/coagulation and purely scattering sulphate
202 aerosols, for the aged plume. Corresponding water vapour perturbations are obtained with radio-
203 sounding observations in western Australia of Fig. 4a (fresh plume, higher section, January 19th;
204 fresh plume, lower section, January 20th; aged plume, February 8th). An additional case is
205 considered for water vapour perturbations in the southern Atlantic Ocean, observations at Saint
206 Helena island of January 25th (see Fig. 4a). The in-plume localised aerosol shortwave (SW)
207 radiative heating and longwave (LW) radiative cooling compensate to a large extent, thus
208 producing very small total aerosol in-plume heating rates. The water vapour LW cooling
209 dominates the localised stratospheric in-plume heating/cooling rates. This produces a very large
210 total plume cooling rate for the higher sections of the fresh plume, reaching values as large as -10
211 K/d. For the lower section of the fresh plume, this cooling is smaller, due to the lesser effective
212 radiative impact of water vapour at lower altitudes; this sums up to a small positive aerosol's
213 heating rate to produce a near-zero total plume heating rate. For the aged plume, both aerosol and
214 water vapour heating/cooling rates are very small due to progressive dilution. The very large
215 cooling rate for the higher section of the fresh plume have produced a rapid descent of this part
216 of the plume, which is estimated at 11.3 K/d in potential temperature from CALIOP during the
217 first week of February and falls to 3.6 K/d during the following weeks due to dilution (Fig. 5d).
218 This radiative cooling is a major forcing for the vertical plume dynamics and its atmospheric
219 dispersion.

220 The top-of-atmosphere (TOA) and surface radiative forcing (RF) of the plume is also estimated,
221 by considering the same cases and both aerosols and water vapour effects. For the fresh plume,
222 the SW and LW aerosol components dominate, producing large instantaneous RF reaching
223 values of -20 Wm^{-2} (TOA) and -28 Wm^{-2} (surface), for the higher section. The aerosol RF
224 component fades rapidly for the aged plume, due to dispersion/dilution. On the contrary, the LW

225 and SW water vapour RF switches from negative to positive values (due to its descent in
 226 altitude) and dominates at TOA for the aged plume. Thus, contrary to what was observed for all
 227 the stratospheric volcanic eruptions of the last 30 years, the HT plume might produce a slightly
 228 positive TOA RF, with a subsequent small warming effect of the climate system. The surface RF
 229 of the aged plume remains dominated by aerosols and reaches negative values as large as almost
 230 -2 Wm^{-2} , which is quite large if compared with recent events. As a point of comparison, the
 231 Raikoke eruption in 2019 and Australian fires 2019-2020 have hemispheric surface RF of about -
 232 0.8 Wm^{-2} (ref. 15) and -2.0 Wm^{-2} (ref. 16), respectively.



233
 234 **Figure 5: Stratospheric radiative cooling due to the HT plume and plume descent.** *Aerosol*
 235 *(panel a), water vapour (panel b) and total plume (panel c) LW (dashed lines), SW (dotted lines)*
 236 *and total (solid lines) radiative heating rates (HR) for the basic cases discussed in the text: fresh*
 237 *plume, higher section (dark red), fresh plume, lower section (red) and aged plume (orange). The*
 238 *additional case of the southern Atlantic profile is presented for water vapour only in panel b*

239 (blue). The CALIOP aerosol observations and water vapour radio-sounding, even if
 240 representative of the same plume sections, are taken at different time intervals (radio-soundings
 241 are taken 2 days later than CALIOP overpasses of the early plume), thus CALIOP profiles are
 242 vertically shifted to match the water vapour enhancements observed with radio-sounding.
 243 CALIOP 532 nm attenuated backscatter ratio (SR) averaged daily over all night traces in the
 244 zonal direction and between 15°S and 25°S in latitude (panel d). The fit is performed over all
 245 pixels where $SR > 4$ and for the two periods Jan 28 - Feb 09 (green line, -11.3 K/d) and Feb 10 -
 246 28 (blue line, -3.6 K/d).

		Fresh plume, higher section	Fresh plume, lower section	Aged plume
TOA	A	-19.4	-12.1	-0.6
	WV	-0.7	-0.4	+0.8
	A+WV	-20.1	-12.5	+0.2
Surface	A	-27.9	-17.5	-1.7
	WV	0.0003	0.0006	0.0018
	A+WV	-27.9	-17.5	-1.7

247 **Table 1: Short-term RF of the HT plume.** TOA and surface RF for the aerosol (A) and water
 248 vapour (WV) plumes, and both (A+WV), for the three cases described in Fig. 5's caption. The
 249 LW and SW RFs are added up in the table. All RF values are in Wm^{-2} .

250 **Methods**

251 *Volcanic plume tracking with geostationary satellite imagers*

252 In order to follow with high temporal and spatial resolution the early stages of the evolution of
 253 the plume, we use a composite RGB product that benefits from the sensitivity of the Himawari-8

254 8.5 μm band to SO_2 and sulphate aerosols. The product is based on the EUMETSAT Ash RGB
255 recipe and uses the brightness temperatures (BT in K) of the three channels: 8.5, 10.4 and 12.3
256 μm . The recipe for the three colour indexes ranging from 0 to 1 is $R = (\text{BT}(12.3) - \text{BT}(10.4) +$
257 $4)/6$, $G = (\text{BT}(10.4) - \text{BT}(0.85) + 4)/9$, $B = (\text{BT}(10.4) - 243)/60$.

258 *Volcanic sulphur dioxide and sulphate aerosols satellite observations with the IMS scheme*

259 The RAL (Rutherford Appleton Laboratory) Infra-red/Microwave Sounder (IMS) retrieval core
260 scheme¹⁷ uses an optimal estimation (OE) spectral fitting procedure to retrieve atmospheric and
261 surface parameters jointly from co-located measurements by IASI (Infrared Atmospheric
262 Sounding Interferometer), AMSU (Advanced Microwave Sounding Unit) and MHS (Microwave
263 Humidity Sounder) on MetOp spacecraft series, using RTTOV 12 (Radiative Transfer for
264 TOVS) as the forward radiative transfer model. The use of RTTOV12 enables the quantitative
265 retrieval of volcanic-specific aerosols (sulphate aerosol) and trace gases (SO_2). The present
266 paper uses IMS SO_2 and sulphate aerosols observations from its near-real time implementation
267 (images can be viewed here: <http://rsg.rl.ac.uk/vistool>). The IMS scheme retrieves the SO_2 in the
268 sensitive region around $\sim 1100\text{-}1200\text{ cm}^{-1}$ (ref. 10). It retrieves sulphate-specific AOD (Aerosol
269 Optical Depth) at $\sim 1200\text{ cm}^{-1}$ (the peak of the mid-infrared extinction cross section¹⁸), assuming
270 a Gaussian extinction coefficient profile shape peaking at 20 km altitude, with 2 km full-width-
271 half-maximum. The bulk of the spectroscopic information on SO_2 and sulphate aerosols, in the
272 IMS scheme, thus comes from the IASI Fourier transform spectrometer, thus we will refer to
273 these observations as IMS/IASI in the following.

274 *Volcanic plumes observations with the CALIPSO-CALIOP space LiDAR*

275 We use attenuated backscatter profiles at 532 nm measured by the CALIOP (Cloud-Aerosol
276 Lidar with Orthogonal Polarisation) spaceborne lidar onboard the CALIPSO (Cloud-Aerosol
277 Lidar and Infrared Pathfinder Satellite Observation) satellite to derive optical properties of the
278 volcanic aerosol plumes. Their AOD is estimated from the ratio of the LiDAR signal at aerosol-
279 free altitudes above and below the volcanic plumes. Aerosol LiDAR ratios are roughly calculated
280 by dividing the AODs by the vertically integrating attenuated backscatter after subtracting
281 molecular backscatter. Finally, LiDAR ratios are used for calculating aerosol extinction profiles
282 using a classic equation¹⁹.

283 *Volcanic plumes observations with the OMPS Limb Sounder*

284 The Ozone Mapping and Profiler Suite Limb Profiler (OMPS-LP) instruments flights onboard
285 the Suomi National Polar-orbiting Partnership (Suomi-NPP) satellite since January 2012. It
286 observes vertical profiles of scattered solar radiation, in the 290-1000 nm spectral range, in a
287 limb-viewing geometry, i.e. tangent to the Earth's atmosphere. We use the aerosol extinction
288 profile inversion algorithm v2.0 (ref. 20) at 675 nm and the integrated stratospheric AOD
289 (SAOD). With respect to previous datasets versions, this dataset exhibits significant retrieval
290 improvements, especially in the Southern Hemisphere (SH), when compared with independent
291 datasets²⁰.

292 *In situ measurements of volcanic aerosol size distributions with LOAC*

293 The Light Optical Aerosol Counter (LOAC) is a multi-angle in situ optical particle²¹ that, thanks
294 to its very limited weight (~300 g), has been operated on small balloon measurement flights at
295 the Observatoire de l'atmosphère du Maïdo at La Réunion island (21.1S, 55.3E), after the HT
296 eruption. Using a laser at 650 nm wavelength, aerosol concentration is derived with LOAC for
297 particles between 150 nm and 30 µm, in 19 size classes. In this work, we show LOAC
298 measurement for January 23rd, 2022 (20-21:30 UTC).

299 *Multi-station analysis of ground-based AERONET sunphotometric data*

300 A multi-station analysis of L1.5 cloud-screened and quality assured sunphotometric data from
301 the AERONET (AErosol RObotic NETwork)²² is carried out at stations in Australia and La
302 Réunion Island, using the VolcPlume portal for the 4D multi-scale monitoring and analysis of
303 volcanic plumes. The contribution with time of the fine (sub-micron) and coarse (super-micron)
304 modes to the total AOD at 500 nm, derived from the spectral deconvolution algorithm²³, is
305 analysed to detect volcanic sulphate aerosols as in ref. 24.

306 *Water vapour observations with radio-sounding*

307 We use water vapour radio-soundings in Western Australia and Saint Helena island.
308 Stratospheric humidity measurements with standard meteorological radio-sounds are particularly
309 challenging due to the low relative humidity and outgassing from the balloon envelope²⁵ which
310 typically contaminates the measurement by tenths of ppmv up to ~100 ppmv at 30 km. However,

311 the exceptionally large relative humidity values found in the HT plume outweigh contamination
312 and uncertainties of Vaisala RS41 radio-sondes used in this work, and the ultra-moist plume
313 clearly stands out of background variability in those soundings. The unusually humid upper
314 stratosphere and its high temperature turn out to be a favourable environment for such
315 measurements. For water vapour sensitive radiative calculations, we remove the systematic
316 impact of sonde outgassing by computing an anomaly with respect to the 90% quantile radio-
317 sonde profile over one month and adding it to a background profile deduced from satellite
318 measurements by Aura MLS.

319 *Radiative forcing and heating/cooling rates modelling with the LibRadtran suite*

320 The clear-sky equinox-equivalent daily-average shortwave (SW, integrated between 300 and
321 3000 nm) and longwave (LW, integrated between 2.5 and 100 μm) surface and top of the
322 atmosphere (TOA) direct radiative forcing (RF) are estimated using the UVSPEC (UltraViolet
323 SPECTrum) radiative transfer model in the libRadtran (library for Radiative transfer)
324 implementation²⁶ and the methodology described in refs. 16 and 27. The SW and LW radiative
325 heating rates are also estimated with UVSPEC/libRadtran, for the same scenarios. Independent
326 cases to account for water vapour and aerosol perturbations associated with the HT eruption are
327 considered. Baseline simulations are obtained with an unperturbed water vapour sounding and a
328 standard background aerosol profile. Volcanic-perturbed simulations are obtained with in-plume
329 water vapour radio-sounding observations and CALIOP aerosol extinction observations, for both
330 fresh (January 16th-20th) and aged plume (February 8th). The spectral variability of the aerosol
331 extinction, and the absorption and angular scattering properties of the aerosol plume are based on
332 hypotheses detailed in Sect. 3.3.

333 **Acknowledgments**

334 This research has been supported by the Agence Nationale de la Recherche (grants no: 21-CE01-
335 0007-01, ASTuS; 21-CE01-0016-01, TuRTLES; 21-CE01-0028-01, PyroStrat; 15-CE04-0003-
336 01, VolcPlume) and the Laboratoire d'Excellence VOLTAIRE (VOLatils – Terre, Atmosphère et
337 Interactions - Ressources et Environnement; ANR-10-LABX-100-01) and CaPPA (Chemical and
338 Physical Properties of the Atmosphere; ANR-11-LABX-0005-01). The providers of the
339 libRadtran suite (<http://www.libradtran.org/>) are gratefully acknowledged. Ghassan Taha,
340 NASA, is gratefully acknowledged for the help with OMPS data. The AERIS thematic centre is

341 acknowledged for the access to CALIOP and Himawari data, and for the development of the
342 VolcPlume Portal, dedicated to the multiscale atmospheric 4D monitoring of volcanic plumes
343 (hosted at AERIS/ICARE Data and Services), whose prototype has been initially developed
344 within the framework of the VolcPlume ANR project (15-CE04-0003-01). M.B. acknowledges
345 support from the European Union's Horizon Europe Framework Programme (HORIZON) FAIR-
346 EASE (grant agreement No. 101058785) and E-shape projects. We thank the AERONET staff
347 and site managers: V. Dufлот (Univ. Réunion), I. Lau and T. Schroeder (CSIRO) for stations at
348 La Réunion and Australia respectively.

349

350 References

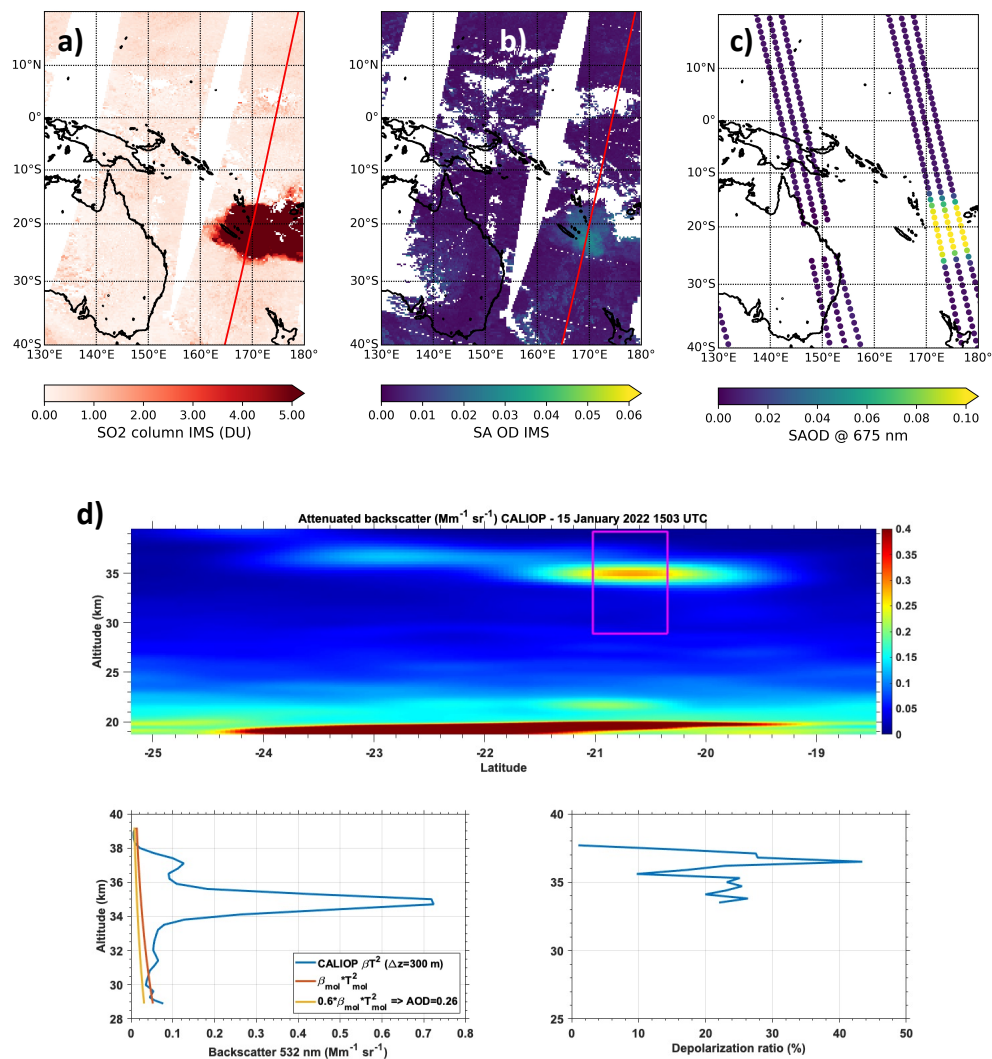
- 351 1. Robock, A. Volcanic eruptions and climate (2000). *Rev. Geophys.* 38(2), 191–219.
352 <https://doi.org/10.1029/1998RG000054>
- 353 2. Solomon, S., Daniel, J.S., Neely, R. R., Vernier, J.-P., Dutton, E .G., Thomason, L.W. (2011),
354 The Persistently Variable Background Stratospheric Aerosol Layer and Global Climate Change,
355 *Science*, 333, 6044, 866-870, doi:10.1126/science.1206027
- 356 3. Andersson, S., Martinsson, B., Vernier, JP. et al. (2015), Significant radiative impact of
357 volcanic aerosol in the lowermost stratosphere. *Nat. Commun.* 6, 7692.
358 <https://doi.org/10.1038/ncomms8692>
- 359 4. Adam, D. (2022), Tonga volcano created puzzling atmospheric ripples, *Nature*, 601, 497. doi:
360 <https://doi.org/10.1038/d41586-022-00127-1>
- 361 5. Wright, C., Hindley, N., M. J. Alexander, M. Barlow, L. Hoffmann, C. Mitchell, F. Prata, M.
362 Bouillon, J. Carstens, C. Clerbaux et al. (2022), Tonga eruption triggered waves propagating
363 globally from surface to edge of space, *Earth and Space Science Open Archive* [preprint], doi:
364 10.1002/essoar.10510674.1.
- 365 6. Carr, J. L., A. Horvath, A., Wu, D. L., Friberg, M. D. (2022), Stereo Plume Height and Motion
366 Retrievals for the Record-Setting Hunga Tonga-Hunga Ha'apai Eruption of 15 January 2022,
367 *Earth and Space Science Open Archive* [preprint], 10, doi: 10.1002/essoar.10510365.1.
- 368 7. Witze, A. (2022), Why the Tongan eruption will go down in the history of volcanology ,
369 *Nature* 602, 376-378, doi: <https://doi.org/10.1038/d41586-022-00394-y>
- 370 8. Guo, S., Bluth, G. J. S., Rose, W. I., Watson, I. M., and Prata, A. J. (2004), Re-evaluation of
371 SO₂ release of the 15 June 1991 Pinatubo eruption using ultraviolet and infrared satellite
372 sensors, *Geochem. Geophys. Geosyst.*, 5, Q04001, doi:10.1029/2003GC000654.

- 373 9. de Leeuw, J., Schmidt, A., Witham, C. S., Theys, N., Taylor, I. A., Grainger, R. G., Pope, R.
374 J., Haywood, J., Osborne, M., and Kristiansen, N. I.: The 2019 Raikoke volcanic eruption – Part
375 1: Dispersion model simulations and satellite retrievals of volcanic sulfur dioxide, *Atmos. Chem.*
376 *Phys.*, 21, 10851–10879, <https://doi.org/10.5194/acp-21-10851-2021>, 2021.
- 377 10. Carboni, E., Grainger, R. G., Mather, T. A., Pyle, D. M., Thomas, G. E., Siddans, R., Smith,
378 A. J. A., Dudhia, A., Koukouli, M. E., and Balis, D. (2016), The vertical distribution of volcanic
379 SO₂ plumes measured by IASI, *Atmospheric Chemistry and Physics*, 16, 4343–4367,
380 <https://doi.org/10.5194/acp-16-4343-2016>.
- 381 11. Sellitto, P., Sèze, G., Legras, B. (2017), Secondary sulphate aerosols and cirrus clouds
382 detection with SEVIRI during Nabro volcano eruption. *International Journal of Remote Sensing*,
383 38 (20), 5657-5672.
- 384 12. Khaykin S., F. Ploeger, A. Podglajen, J.-U. Grooß, F. Tence, A. Baron, K. Khlopenkov, K.
385 Bedka, S. Bekki, V. Duflot, S. Godin-Beekmann, J. Jumelet, B. Legras, R. Querel, T. Saka, P.
386 Sellitto, G. Taha et al. (2022), Major and persistent perturbation of stratospheric water budget
387 produced by Hunga Tonga eruption, in prep.
- 388 13. Vehkamäki, H., Kulmala, M., Napari, I., Lehtinen, K. E. J., Timmreck, C., Noppel, M., and
389 Laaksonen, A. (2002), An improved parameterization for sulfuric acid–water nucleation rates for
390 tropospheric and stratospheric conditions, *J. Geophys. Res.*, 107(D22), 4622,
391 [doi:10.1029/2002JD002184](https://doi.org/10.1029/2002JD002184).
- 392 14. Khaykin, S., Legras, B., Bucci, S., Sellitto P., et al. (2020), The 2019/20 Australian wildfires
393 generated a persistent smoke-charged vortex rising up to 35 km altitude, *Commun. Earth*
394 *Environ.* 1, 22, <https://doi.org/10.1038/s43247-020-00022-5>.
- 395 15. Kloss, C., Berthet, G., Sellitto, P., Ploeger, F., Taha, G., Tidiga, M., Eremenko, M.,
396 Bossolasco, A., Jégou, F., Renard, J.-B., and Legras, B. (2021) Stratospheric aerosol layer
397 perturbation caused by the 2019 Raikoke and Ulawun eruptions and their radiative forcing,
398 *Atmos. Chem. Phys.*, 21, 535–560, <https://doi.org/10.5194/acp-21-535-2021>.
- 399 16. Sellitto, P., Belhadji, R., Kloss, C., and Legras, B. (2022), Radiative impacts of the
400 Australian bushfires 2019–2020 – Part 1: Large-scale radiative forcing, *EGUsphere* [preprint],
401 <https://doi.org/10.5194/egusphere-2022-42>.
- 402 17. Siddans, R. (2019) Water Vapour Climate Change Initiative (WV_cci) - Phase One,
403 Deliverable 2.2; Version 1.0, 27 March 2019,
404 [https://climate.esa.int/documents/1337/Water_Vapour_CCI_D2.2_ATBD_Part2-](https://climate.esa.int/documents/1337/Water_Vapour_CCI_D2.2_ATBD_Part2-IMS_L2_product_v1.0.pdf)
405 [IMS_L2_product_v1.0.pdf](https://climate.esa.int/documents/1337/Water_Vapour_CCI_D2.2_ATBD_Part2-IMS_L2_product_v1.0.pdf)
- 406 18. Sellitto, P. and Legras, B. (2016), Sensitivity of thermal infrared nadir instruments to the
407 chemical and microphysical properties of UTLS secondary sulfate aerosols, *Atmos. Meas. Tech.*,
408 9, 115–132, <https://doi.org/10.5194/amt-9-115-2016>.

- 409 19. Fernald, F. G., (1984), Analysis of atmospheric lidar observations: some comments, *Appl.*
410 *Opt.* 23, 652-653
- 411 20. Taha, G., Loughman, R., Zhu, T., Thomason, L., Kar, J., Rieger, L., and Bourassa, A. (2021),
412 OMPS LP Version 2.0 multiwavelength aerosol extinction coefficient retrieval algorithm,
413 *Atmos. Meas. Tech.*, 14, 1015–1036, <https://doi.org/10.5194/amt-14-1015-2021>.
- 414 21. Renard, J.-B., Dulac, F., Berthet, G., Lurton, T., Vignelles, D., Jégou, F., Tonnelier, T.,
415 Jeannot, M., Couté, B., Akiki, R., Verdier, N., Mallet, M., Gensdarmes, F., Charpentier, P.,
416 Mesmin, S., Duverger, V., Dupont, J.-C., Elias, T., Crenn, V., Sciare, J., Zieger, P., Salter, M.,
417 Roberts, T., Giacomoni, J., Gobbi, M., Hamonou, E., Olafsson, H., Dagsson-Waldhauserova, P.,
418 Camy-Peyret, C., Mazel, C., Décamps, T., Piringier, M., Surcin, J., and Daugeron, D. (2016),
419 LOAC: a small aerosol optical counter/sizer for ground-based and balloon measurements of the
420 size distribution and nature of atmospheric particles – Part 1: Principle of measurements and
421 instrument evaluation, *Atmos. Meas. Tech.*, 9, 1721–1742, [https://doi.org/10.5194/amt-9-1721-](https://doi.org/10.5194/amt-9-1721-2016)
422 2016.
- 423 22. Holben, B., Eck, T., Slutsker, I., Tanré, D., Buis, J., Setzer, A., Vermote, E., Reagan, J.,
424 Kaufman, Y., Nakajima, T., Lavenu, F., Jankowiak, I., and Smirnov, A. (1998), AERONET – A
425 federated instrument network and data archive for aerosol characterization, *Remote Sens.*
426 *Environ.*, 66, 1–16, doi:10.1016/S0034-4257(98)00031-5.
- 427 23. O’Neill, N., Eck, T., Smirnov, A., Holben, B., and Thulasiraman, S. (2003), Spectral
428 discrimination of coarse and fine mode optical depth, *J. Geophys. Res.-Atmos.*, 108, 4559,
429 doi:10.1029/2002JD002975.
- 430 24. Boichu, M., Chiapello, I., Brogniez, C., Péré, J.-C., Thieuleux, F., Torres, B., Blarel, L.,
431 Mortier, A., Podvin, T., Goloub, P., Sohne, N., Clarisse, L., Bauduin, S., Hendrick, F., Theys, N.,
432 Van Roozendaal, M., and Tanré, D.: Current challenges in modelling far-range air pollution
433 induced by the 2014–2015 Bardarbunga fissure eruption (Iceland), *Atmos. Chem. Phys.*, 16,
434 10831-10845, <https://doi.org/10.5194/acp-16-10831-2016>, 2016.
- 435 25. Vömel H., V. Yushkov, S. Khaykin, L. Korshunov, E. Kyrö, and R.Kivi (2007),
436 Intercomparisons of stratospheric water vapor sensors: FLASH-B and NOAA/CMDL frost point
437 hygrometer, *J. Atmos. Oceanic Technol.*, 24, 941–952
- 438 26. Emde, C., Buras-Schnell, R., Kylling, A., Mayer, B., Gasteiger, J., Hamann, U., Kylling, J.,
439 Richter, B., Pause, C., Dowling, T., and Bugliaro, L. (2016), The libRadtran software package
440 for radiative transfer calculations (version 2.0.1), *Geosci. Model Dev.*, 9, 1647–1672,
441 <https://doi.org/10.5194/gmd-9-1647-2016>.
- 442 27. Sellitto, P., di Sarra, A., Corradini, S., Boichu, M., Herbin, H., Dubuisson, P., Sèze, G.,
443 Meloni, D., Monteleone, F., Merucci, L., Rusalem, J., Salerno, G., Briole, P., and Legras, B.
444 (2016), Synergistic use of Lagrangian dispersion and radiative transfer modelling with satellite
445 and surface remote sensing measurements for the investigation of volcanic plumes: the Mount

446 Etna eruption of 25–27 October 2013, Atmos. Chem. Phys., 16, 6841–6861,
447 <https://doi.org/10.5194/acp-16-6841-2016>, 2016.

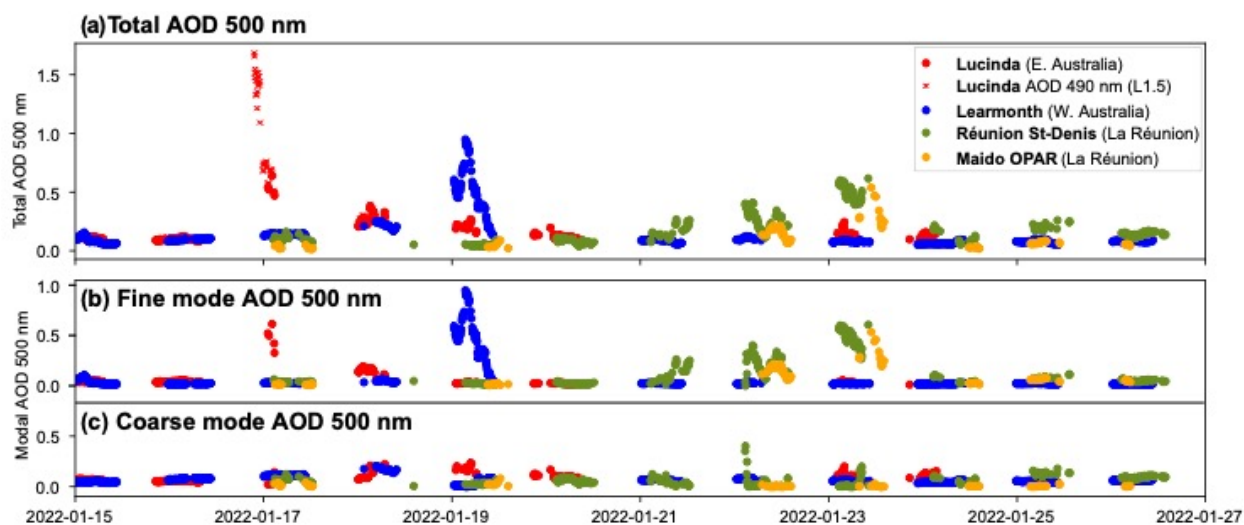
448 Supplementary Information



449

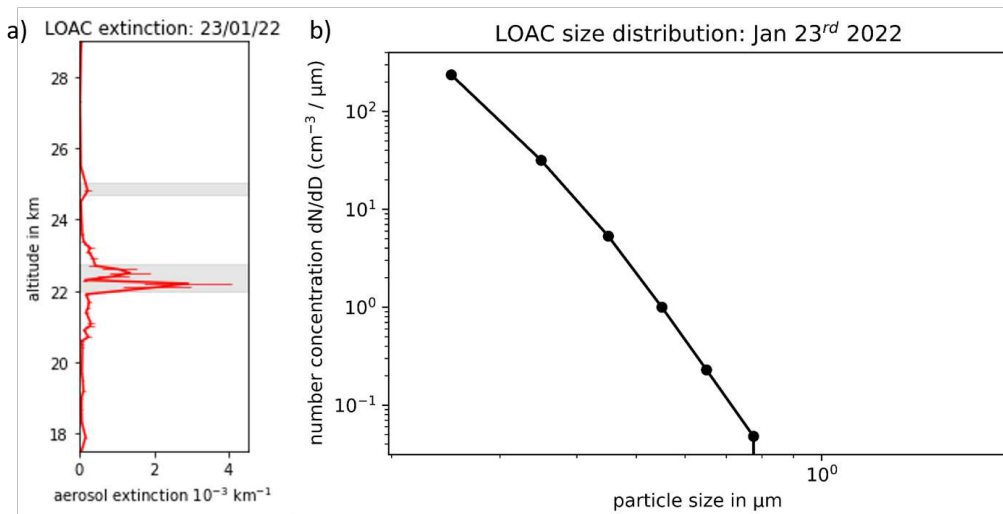
450 **Figure S1. IMS/IASI SO₂ (panel a) and sulphate-specific AOD (panel b) observations for**
451 **January 15th. In panel a and b, the red line is CALIOP track for the same day. OMPS-LP**
452 **integrated stratospheric optical depth (panel c) for January 16th. Attenuated CALIOP**
453 **backscatter at 532 nm, corrected transmission and depolarization ratio (panel d) in the**

454 identified plume section (pink squares). The CALIOP track in panels d is the one identified
 455 in panels a and b.



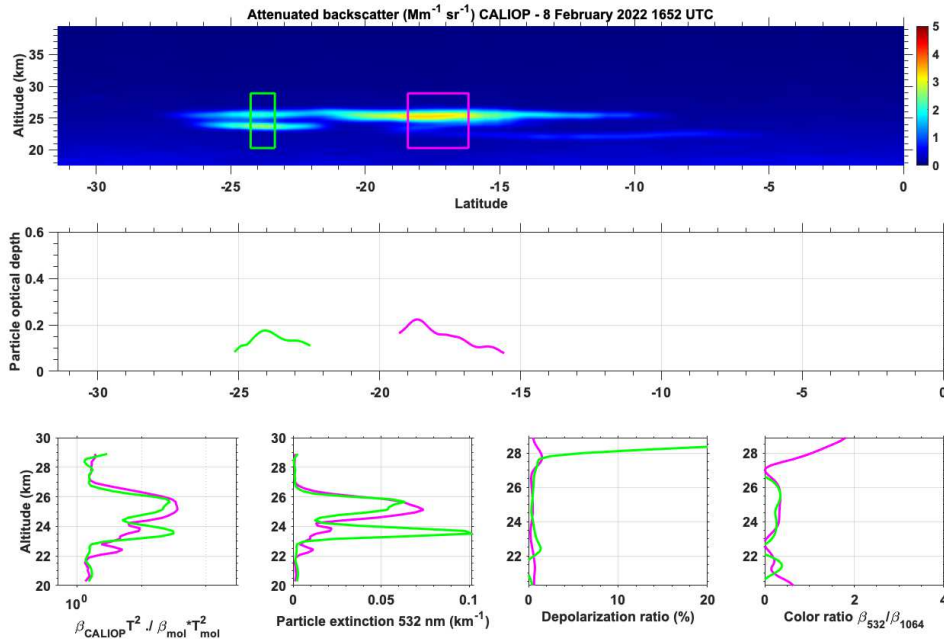
456

457 **Figure S2.** Total AOD at 500 nm (panel a), and corresponding fine mode (panel b) and
 458 coarse mode AOD (panel c), for Lucinda, Australia (red dots), Learmonth, Australia (blue
 459 dots), Réunion Saint-Denis and Maïdo OPAR, La Réunion island, Oversea French
 460 Territories (green and yellow dots) AERONET stations.



461

462 **Figure S3.** In situ LOAC extinction profile at 532 nm (panel a) and size distribution (panel
 463 **b)** for observations at La Réunion island on January 23rd, 2022 (rapid-response campaign
 464 following HT eruption).



465

466 **Figure S4.** Attenuated CALIOP backscatter at 532 nm, and integrated plume's AOD,
 467 corrected transmission, extinction, depolarization and colour ratio in the two identified
 468 plumes sections (pink and green squares), for February 8th, 2022. The CALIOP track is
 469 overpassing eastern Australia, similar to Fig. 2.